Low-loss GaN-on-insulator platform for integrated photonics

M. GROMOVYI,[1,4] M. EL KURDI,[1] X. CHECOURY,[1] E. HERTH,[1] F. TABATABA-VAKILI,[1,3] N. BHAT,[2] A. COURVILLE,[2] F. SEMOND,[2] AND P. BOUCAUD[2,5]

[1]*Université Paris-Saclay, CNRS, C2N, 10 boulevard Thomas Gobert, 91120 Palaiseau, France*
[2]*Université Côte d'Azur, CNRS, CRHEA, Rue Bernard Grégory, 06905 Sophia-Antipolis, France*
[3]*Currently with Fakultät für Physik, Munich Center for Quantum Science and Technology (MCQST), and Center for NanoScience (CeNS), Ludwig-Maximilians-Universität München, Geschwister-Scholl-Platz 1, 80539 München, Germany*
[4]*maksym.gromovyi@universite-paris-saclay.fr*
[5]*philippe.boucaud@crhea.cnrs.fr*

Abstract: III-Nitride semiconductors are promising materials for on-chip integrated photonics. They provide a wide transparency window from the ultra-violet to the infrared that can be exploited for second-order nonlinear conversions. Here we demonstrate a photonics platform based on epitaxial GaN-on-insulator on silicon. The transfer of the epi-material on SiO_2 is achieved through wafer bonding. We show that quality factors up to 230 000 can be achieved with this platform at telecommunication wavelengths. Resonant second harmonic generation is demonstrated with a continuous wave conversion efficiency of 0.24%/W.

1. Introduction

Integrated nonlinear optics offers wide variety of opportunities for creating useful quantum and classical on-chip light sources such as optical parametric oscillators [1], frequency combs [2], and heralded single photon sources [3]. Integration of light sources on chip provides an important light confinement in the waveguides and often additional cavity field enhancement in the resonator geometries such as rings or photonic crystals. Both light confinement and cavity field enhancement lead to high power densities, which are extremely beneficial for efficient nonlinear processes. To date, numerous platforms for integrated nonlinear optics have been studied including $LiNbO_3$, GaAs, GaP, GaN, AlN and of course Si [4–11], which remains a champion that clearly benefits from a mature Complementary-Metal-Oxide Semiconductor (CMOS) technology. All these platforms have their advantages and disadvantages and offer variable nonlinear efficiencies and integration densities depending on the values of the nonlinear coefficients and on the refractive index contrast. An additional limiting factor is related to losses which are both determined by the quality of the grown material and by the maturity of the fabrication process such as roughness and the absorption of the surface passivation layer. Although in the longer term, the growth and fabrication quality for all these materials will eventually level up, there still remains one important limiting factor that clearly separates them regarding high power densities, namely two photon absorption (TPA). TPA is determined by the band gap of the materials and by the working wavelength, which is often in the telecom range due to the historically developed infrastructure of sources, detectors, etc. In this regard, small band gap semiconductors such as Si and GaAs are fundamentally limited and there seems to be no way around this problem other than to change the working wavelength and all the surrounding infrastructure.

In this light, wide band gap III-N semiconductors can play an important role in integrated nonlinear optics since they can offer relatively high $\chi^{(2)}$ second-order nonlinearities while not

suffering from strong two-photon absorption at telecom wavelengths. Historically, these materials have been suffering from high losses due to poor growth quality and process technology in comparison to Si. Recently, however, an important progress has been made in the epitaxially-grown AlN-on-sapphire platform leading both to a record second harmonic generation (SHG) efficiency [12] and to the first demonstration of an integrated optical parametric oscillator (OPO) with AlN ring resonators [13]. Meanwhile GaN, a major III-Nitride material, can offer a higher $\chi^{(2)}$ nonlinear coefficient as compared to AlN but up to now remained in the shadow of AlN due to high losses reported so far. At telecommunication wavelengths, the absolute value of the second-order nonlinear coefficient for AlN is around 6 pm/V [14] whereas it is around 16 pm/V for GaN [15]. As the nonlinear processes scale with the square of this parameter, the advantage of using GaN as the core material of the III-nitride photonics platform is thus substantial.

In this work, we address the issue of optical losses with GaN and show that epitaxial GaN thin films can be reliably transferred onto oxide on a silicon substrate and at the same time demonstrate 10 times improvement in terms of losses compared to the previously demonstrated GaN-on-insulator platform [11]. We also demonstrate resonant second harmonic conversion efficiency of 0.24%/W that represents as well an improvement as compared to the value of 1.5×10^{-2}%/W reported in Ref. [11] with a similar platform. The transfer of the III-nitride onto oxide allows one to avoid the use of air-suspended structures for optical confinement [15–18]. The III-nitrides used in this work are grown on a silicon substrate, enabling an upper scaling of the platform to 8 or even 12 inches substrates. The results presented here open up the prospect of future high-efficiency, low-loss nonlinear photonic devices made of GaN that can be integrated into silicon and are compatible with the silicon-based process environment.

2. Fabrication

The initial structure was grown by ammonia-assisted molecular beam epitaxy (MBE) on 2-inch double-side polished Si(111) wafer. First, a 150 nm thick AlN buffer layer was grown at 1040°C prior to the growth of the main active 520 nm thick GaN layer at 780°C. The AlN buffer layer is needed in order to initiate the proper growth of GaN on Si(111) and to compensate for the residual tensile stress, that occurs when cooling from growth temperature to room temperature. Despite the small thickness and simplicity of the vertical stacking, the X-Ray diffraction measurement for similar structures gives the following parameters for the GaN (002) - 1200'' (0.33° full width at half maximum) and GaN (302) - 2400'' (0.66° full width at half maximum) indicating a good material quality.

Atomic force microscopy (AFM) measurement of the surface roughness (σ) of the as-grown sample gives a root-mean-square (rms) value of 2.6 nm and a typical lateral scale (Λ) of about 300 nm for 10 μm by 10 μm scans (Fig. 1(a)). A simple Payne-Lacey model [19] shows that this roughness makes a negligible impact at 1.5 μm but can lead to significant propagation losses in the visible range as it was already experimentally confirmed in Ref. [20]. Therefore, an additional 60 nm thick GaN layer was overgrown on top of the initial structure using metal organic vapor phase epitaxy (MOVPE). This allowed to drastically reduce the amplitude of the surface roughness down to 1.0 nm (rms value of 1.3 nm for 10 μm x 10 μm scans) and increase the typical lateral scale of roughness as shown in Fig. 1(b) preventing the coupling between the guided and the radiation modes.

Epitaxial GaN layers exhibit both very high quality of the bulk material and smooth surface, but since they are grown on Si, they do not directly present a guiding layer because Si has a larger refractive index than GaN. Previously, we and other groups have studied membrane-type structures in forms of microdisks and photonic crystals by under-etching the Si with the Xenon difluoride (XeF$_2$) gas [15–18]. This is an interesting solution but it has its limitations since it restricts the possibilities of GaN integration on a Si platform. Additionally, the nanotethers, required to suspend the structures, introduce propagation losses. Thermal dissipation of suspended structures
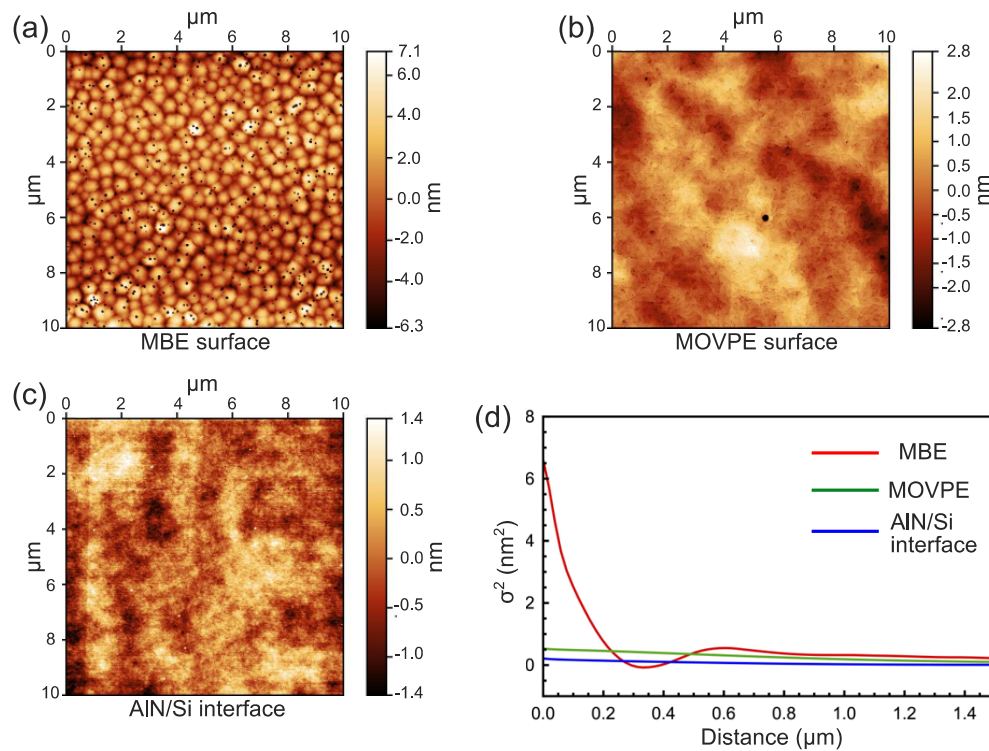
Fig. 1. (a) $10 \times 10 \; \mu m^2$ AFM image showing the GaN surface roughness (2.6 nm rms) after MBE growth. (b) $10 \times 10 \; \mu m^2$ AFM image of GaN surface after MOVPE regrowth of an additional 60 nm GaN layer, the roughness is significantly reduced with a typical rms = 1.3 nm. (c) $10 \times 10 \; \mu m^2$ AFM image of N-polar AlN surface after Si substrate removal, the surface is very smooth with a typical rms = 0.46 nm. (d) Autocorrelation function of roughness amplitude (σ) for the three cases.

is not as efficient as the one of bulk or encapsulated structures. Undesirable bending of the suspended tapers can also introduce additional losses.

The goal of this article is to demonstrate that the high quality GaN epitaxial layers can be transferred on an oxide (SiO_2) while preserving low losses of the photonic structures. The process flow is presented in Fig. 2. In order to do the transfer, first we have deposited a 2.2 µm thick SiO_2 layer on top of GaN using plasma-enhanced chemical vapor deposition (PECVD). Next, we evaporate Ti/Au layers on top of the SiO_2. The same metals were also deposited on the support Si handle wafer since these layers are needed for the wafer bonding which was performed in a commercial bonder. The sample with the active GaN layer and the Si support wafer were bonded through the metal interface by applying the required pressure at a temperature of about 320°C. The 2.2 µm thick SiO_2 layer was needed in order to form a waveguide and to isolate the active GaN layer from the metal and the Si(100) substrate that serves here as a carrier. It should be noted that an alternative solution for bonding is as well available in the future using benzocyclobutene (BCB) instead of gold. Depending on the application geometry, thinner layers of the buffer oxide may be used and coupling between III-N and Si photonic structures can be realized.

After bonding, we removed the initial Si substrate, which is in direct contact with the active layers. For this purpose, we have used an inductively-coupled plasma (ICP) etching reactor adapted for deep Si etching using fluorine gases. The initially-polished Si substrate was
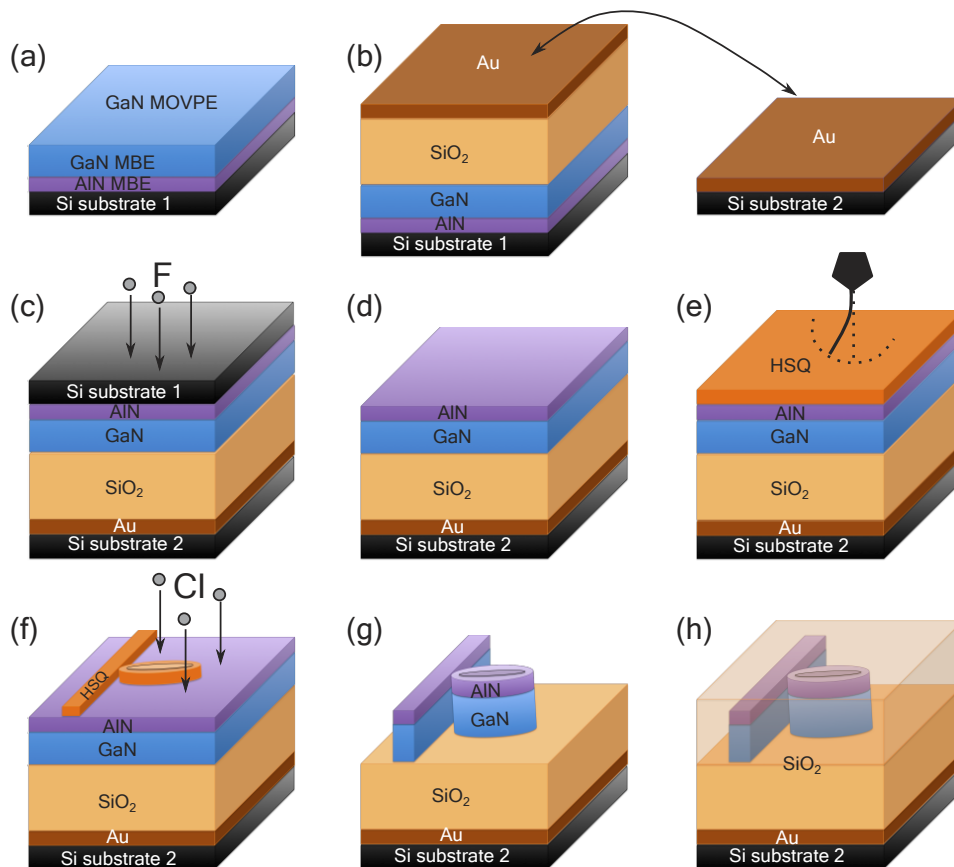
Fig. 2. (a) Initial growth of the III-nitride layer by MBE with the subsequent MOVPE smoothing. (b) Deposition of SiO$_2$ optical cladding and Ti/Au layer for the wafer bonding. (c) Wafer bonding followed by Si substrate removal by ICP deep etching. (d) III-N layer successfully reported on the SiO$_2$/Si substrate. (e) HSQ spin coating and e-beam writing. (f) HSQ mask used for chlorine-based etching of the AlN/GaN layers. (g) III-nitride etched photonic structure on the SiO$_2$ optical cladding layer. (h) Final structure after SiO$_2$ encapsulation.

successfully removed with a highly selective etching process between AlN and Si (1/1000). The final AlN surface after removal of the Si substrate exhibits some macroscopic defects related to micromasking. It should be emphasized that the density of these defects is relatively small ($0.1/\mu m^2$) and the AlN surface is otherwise extremely smooth with a rms of 0.46 nm for 10 µm by 10 µm surface as shown in Fig. 1(c), demonstrating the successful transfer of the epitaxial GaN layer. This smoothness is as well highlighted on the autocorrelation function of the surface roughness, as seen in Fig. 1(d).

GaN-on-oxide naturally forms a planar guiding layer while oxide serves as an optical cladding that isolates our active layer from the metal interface and the Si support substrate. In order to evaluate the photonic quality of this structure, we have fabricated ring resonators coupled to bus waveguides as shown in the optical microscopy image in Fig. 3(a). The diameter of the microrings is 90 µm. The width of the ring is 1.1 µm. The access waveguides have a width of 1.3 µm. This width is reduced to 0.9 µm close to the microring resonator. The geometry was defined using an electron-beam lithography equipment operating at 80 kV. Lithography was performed with a 400 nm thick Hydrogen SilsesQuioxane (HSQ) negative electronic resist. After electron beam (e-beam) insolation and the development processes, the HSQ resist was thermally annealed and stabilized in an O_2 plasma so that it could be used as a mask for the semiconductor etching. The AlN/GaN layers were etched using chlorinated gases in an ICP dry etching plasma reactor. We observe the overall verticality to be about 76 degrees while it is even better (85 degrees) in the coupling gaps between the rings and the waveguides, as shown in the SEM images of Fig. 3(b-c). Once the semiconductors were etched, the residual HSQ resist was removed in a fluorine-based plasma in a capacitively-coupled plasma (CCP) reactor. Finally, we symmetrized the structure by depositing 2.5 µm of SiO_2 by PECVD. Figure 3(d) shows scanning electron microscopy (SEM) images of the final structure and its cross-section as it was cleaved after the optical measurements.

One could obviously add an additional etching step in order to remove, if needed, the AlN top layer in order to keep an active layer for nonlinear photonics with the largest nonlinear susceptibility. We first note that the thickness of the AlN layer can be smaller than 150 nm, as reported in this work, and even below 100 nm while still keeping a good material quality for samples grown by molecular beam epitaxy. The AlN buffer layer might thus represent a small fraction of the total thickness. The additional etching step that requires a good control of etching rate could be performed by the same ICP dry etching equipment or by atomic layer etching. One needs to ensure that plasma dry etching of AlN does not induce plasma damages i.e. increase the layer roughness that can be detrimental for optical scattering. It explains why we did not attempt this procedure here. The best results might be expected with atomic layer etching.
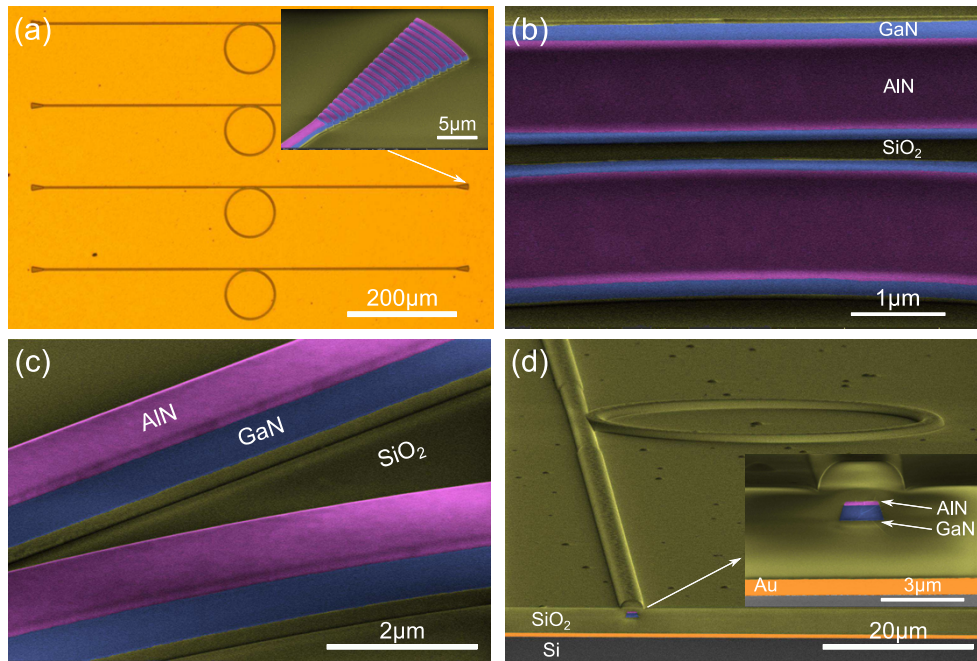
Fig. 3. (a) Microscope image of a general view of the fabricated structures. The inset shows a SEM image of the gratings. (b) SEM image showing a view of a gap between the bus waveguide and a ring resonator. (c) SEM images of smooth GaN walls after ICP etching. (d) SEM images showing a general view of a fabricated structure with a zoom of a cleaved facet. All images are represented in false colors.

3. Optical characterizations

In order to characterize the fabricated ring resonators, we have performed standard transmission experiments. We used a TUNICS laser source with a fiber output, tunable in the 1600–1680 nm telecom range.

The ring resonators are coupled to a bus waveguide with gratings on both ends of the waveguides for laser in and out-coupling. The grating period is 1.05 µm divided into 0.63 µm GaN and 0.42 µm for SiO_2, as shown in the inset of Fig. 3(a) before encapsulation. It should be noted that the optical measurements were performed for the resonators both with and without SiO_2 encapsulation layer. Therefore, we have worked with a reduced coupling efficiency varying between −10 dB without SiO_2 layer and −15 dB with the encapsulation layer. The goal of this experiment was only to analyze the quality factors of the ring resonators and not to optimize the coupling efficiency. Moreover, this experiment does not require high power and high coupling efficiencies. Alternatively, end-fire coupling would provide a more efficient coupling solution but it would be difficult to perform the measurements both before and after SiO_2 deposition in this case.

After optimizing both in- and out-coupling between fibers and gratings, the wavelength scan was performed over a 30 nm spectral range and the output power was measured with a photodiode detector synchronized with the laser scanning. Figure 4(a) depicts an example of such a scan. Here we can see small background variation of the output power and a significant drop in transmission efficiency at specific wavelengths. The background variation comes from the varying coupling efficiency of the gratings and complex Fabry-Perot resonances between the 800 µm long waveguide with two coupling gratings on both ends. The deep drop in the transmission

is due to the resonant frequencies of the rings. The 5 nm free spectral range perfectly corresponds to the TE00 modes in the 90 μm diameter ring. Figure 4(b) shows a zoom-in on a particular transmission resonance dip. We can deduce the loaded quality factor by performing a Lorentzian fit of the resonance, as it is shown in Fig. 4(b). This estimation gives access to the loaded quality factor $1/Q_{loaded} = 1/Q_{intrinsic} + 1/Q_{coupling}$, which consists of the intrinsic quality factor of the ring determined by the intrinsic losses in the ring and the coupling quality factor determined by the losses arising from the coupling between the ring and the waveguide.
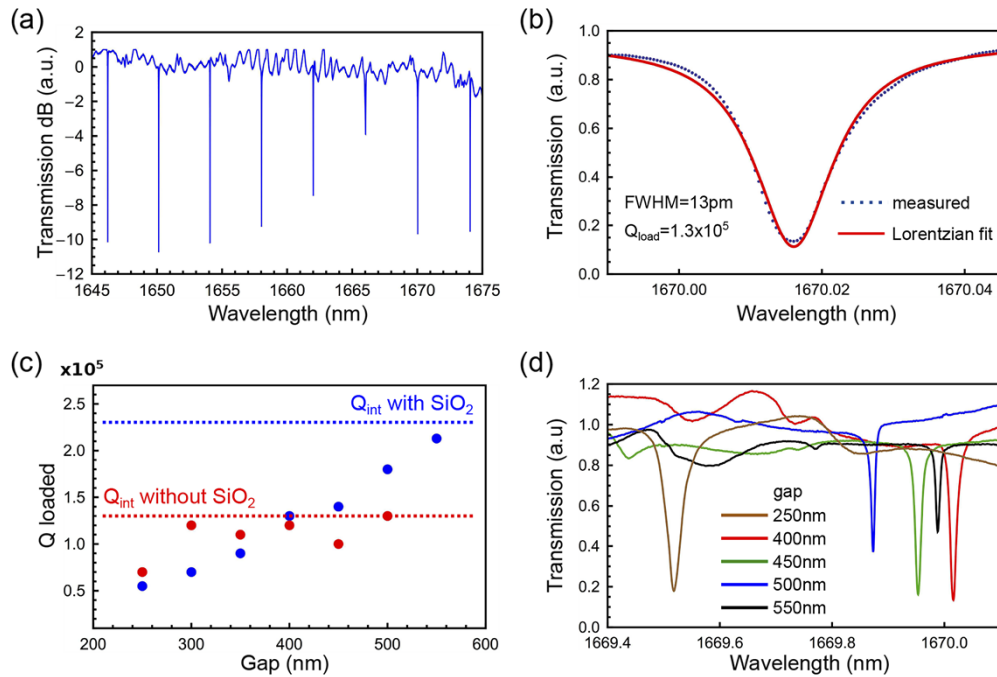
Fig. 4. (a) An example of the transmission spectrum of a 90 μm diameter ring resonator. (b) A zoom of one given resonance with its Lorentzian fit. (c) Loaded quality factor as a function of the coupling gap with deduced quality factors both before and after SiO_2 encapsulation of the ring resonators. (d) Transmission curve for the 1670 nm resonance for different coupling gap distances.

Light is injected into the resonator by the evanescent coupling in a small gap between the waveguide and the ring (see Fig. 3(b)). The injection efficiency depends both on the coupling, mainly determined by the size of the gap, and the intrinsic quality factor of the ring resonator. The injection can increase to 100% for the so-called critical coupling when the quality factor of the coupling equals the intrinsic quality factory of the ring $1/Q_{coupling} = 1/Q_{intrinsic}$. By studying the transmission spectra for the different structures with the coupling gaps varying from 250 up to 550 nm, we can observe the evolution of the transmission and the loaded quality factors for these structures as shown on Fig. 4(d). Using basic models described in Ref. [21], we can deduce the intrinsic quality factors for our resonators according to: $Q_{intrinsic} = 2Q_{loaded}/(1 \pm \sqrt{T_0})$, T_0 being the normalized transmitted power at the resonance wavelength, the minus sign corresponding to the over-coupled regime and the plus sign corresponding to the under-coupled regime.

The measurements described above were performed on the same sample both before and after SiO_2 encapsulations. In Fig. 4(c), we can see that prior to the SiO_2 deposition we quickly reach the under-coupled regime by increasing the coupling gap above 300 nm. In this case the loaded quality factor tends towards intrinsic quality factor of the ring estimated to be around

Q_{int} = 130 000. This is already a very good result in comparison to the previously reported GaN-on-insulator structures [7]. We were able to reach even better performance after the resonators were encapsulated with 2.5 μm thick SiO_2 layer. For this type of structure and following the evolution of the injection efficiency as a function of the coupling gap, we can clearly observe the transition from the over-coupled to under-coupled regime going through the near-critical coupling at Q_{loaded} = 115 000, which allows us to estimate the intrinsic quality factor as Q_{int} = 230 000 – record result for this type of GaN structures transferred to an oxide substrate. The thickness of the bonding oxide layer (2.2 μm) ensures that the observed losses are not due to the metallic bonding layer, as confirmed by a 1-D modeling of the slab waveguide that does not indicate significant overlap and losses between the optical mode and the metallic bonding layer.

A significant improvement of the intrinsic quality factor of the ring after the SiO_2 encapsulation suggests that the waveguide sidewall roughness still remains the main source of propagation losses. Indeed, the reduction of the index contrast at the waveguide/cladding interfaces allows to reduce the impact of this roughness on the coupling between the guided and the radiation modes of the ring and improves its quality factor. We emphasize that the results were obtained with a relatively thin III-nitride layer (730 nm for the III-nitride stack in this study) while layers with a thickness larger than 1 μm are usually used in the literature. The thickness is here limited by the appearance of cracks when using only AlN and GaN bilayers. Larger thicknesses could be achieved by growing more complex heterostructures. Previous studies for a similar AlN-on-insulator platform show that even further improvement could be expected after high-temperature annealing of the structure that would allow reducing the residual absorption in the PECVD-quality SiO_2 layer [2]. Although we could not take advantage of this approach since high-temperature annealing is limited by the mechanical stability of the bonded layers, the present work remains a very good result in terms of propagation losses and is the best reported to the best of our knowledge. An alternative option to replace the PECVD SiO_2 in order to minimize the optical losses could be to use oxides grown by low-pressure chemical vapor deposition or a silicon handle substrate with a thick thermal oxide.

Direct growth of GaN on sapphire can offer as well high intrinsic quality factors [22–24]. The crystalline quality of GaN might be in some cases better on sapphire than on silicon since the strain issues associated with the mismatch of thermal dissipation coefficients are relaxed. The difference in material quality on silicon or on sapphire is nonetheless dependent on the material thickness. For materials with an equivalent 750 nm thickness as reported in this work, one cannot take advantage of a 3D to 2D growth mode and the difference between sapphire or silicon substrates is not so stringent. Developing a platform with III-nitrides on a silicon substrate exhibits nonetheless specific advantages as compared to photonic circuits on sapphire. A key feature for photonic circuits is the co-integration or hetero-integration of multiple functionalities. Many options are available with silicon substrates as silicon photonics is a mainstream technology, one basic advantage being its compatibility with the CMOS environment and the processing tools. On the contrary, sapphire is rather a stand-alone platform without the opportunity to bring easily control electronics on chip. The electronics integration is one additional asset to benefit from the specific features of III-nitrides like Pockels or piezoelectric effects through high-frequency modulations. Starting from III-nitrides grown on silicon offers as well the advantage of epitaxial growth on large substrates, up to 300 mm. The transfer of III-nitrides grown on silicon is moreover easier as compared to III-nitride on sapphire that requires laser lift-off of sapphire substrate and leads to a less-controlled interface in terms of roughness [25]. This is a direct consequence of the laser beam inhomogeneity and its serial scanning that lead to physical damages and residues. The index contrast for III-nitrides on oxide (n ~1.45 at 1550 nm) is larger as compared to III-nitrides on sapphire (n ~1,74 at 1550 nm) thus allowing a better modal confinement and smaller bending radius for waveguides and microrings while minimizing radiation losses. It is thus an opportunity to engineer more compact photonic circuits. The bonding process allows as well one to manage

the interface between substrate and the first epi-layer, the AlN layer in this case. Defects are specifically located at this interface and can lead to short non-radiative lifetimes, detrimental to the recombination dynamics in lasers [26].

4. Second harmonic demonstration

In order to highlight the interest of the GaN-on-insulator on silicon platform for nonlinear photonics, we have investigated second harmonic generation with the microring cavities. The experiments were performed at room temperature under continuous wave excitation. The injection of the pump laser was achieved through a cleaved facet. The second harmonic signal was collected through the opposite cleaved facet following its propagation through the bus waveguide. As compared to the structures shown in Fig. 3(a), we did not use the gratings for light coupling but facets as shown in Fig. 3(d). The harmonic signal was collected through the same bus waveguide as for pump injection. This is not an ideal case since the coupling distance around 800 nm is very different from the coupling at 1600 nm. We did simultaneously record the harmonic signal with a camera as seen perpendicularly to the propagation plane. Specific filters were used to reject the pump and ensure that the collected signal is indeed at twice the frequency of the pump signal. For some structures, the width of the ring was varied by steps of 1 nm, thus allowing one to look for phase matching. The microrings were indeed designed (ring width) in order to be as close as possible from phase matching. We did investigate both TE and TM polarizations for pump injection.

The second harmonic experiments were performed by investigating the pump wavelength variations and the width of the rings. Figure 5 shows the results as obtained with the camera following this multi-parameter investigation. Figure 5(a) shows images recorded from the top surface for a specific microring as the pump laser is tuned to match resonances in the transmission dip as shown in Fig. 4(a). The labeling of the resonances corresponds to the one shown in Fig. 5(c). A series of resonances is thus investigated. For all structures, we can observe a spot at the output of the waveguide corresponding to scattered harmonic light. The brightness of the spot varies significantly as a function of the pump resonance. The brightness is maximal for the resonance at 1676.018 nm. In the latter case, the scattered second harmonic signal can be clearly observed as well on the microring. Figure 5(b) shows an image of the harmonic signal for an optical pump tuned on resonance 3 for microrings with different widths. The microring width varies by steps of 1 nm around 775 nm. There is clearly a very strong dependence of the harmonic signal as a function of the microring width, with a signal that vanishes when the width deviates by more than 2 nm.

The same results can be quantitatively analyzed as shown in Fig. 5(d) and (e). Figure 5(d) shows the SHG conversion efficiency in %/W as a function of the ring width. It corresponds to the data shown in Fig. 5(b). A more global view of the harmonic conversion efficiency for the different resonances is shown in Fig. 5(e) and for the different ring widths. The conversion efficiency was obtained from the ratio of the harmonic power outcoupled from the microring to the waveguide and the square of the pump signal injected into the microring. We did account for typically a 10 dB coupling loss at the facet and propagation through the waveguide for the pump. A typical 10 dB coupling loss was as well considered for the propagation of the harmonic through the output waveguide and the out-coupling from the facet. In each case we did account for the specific coupling losses as measured for each structure. The striking feature is that the conversion efficiency is highly resonant and becomes significant up to 0.24%/W for only one resonance and one microring width. As illustrated as well in Fig. 5(d), the conversion efficiency drops significantly when the microring width is varied by only 1 nm. This resonant behavior is a direct indication that we are close to the doubly resonant phase matching conditions This resonant character is further evidenced quantitatively in Fig. 5(e) where we see that the resonance enhancement only occurs for one specific resonance. The double resonance condition both for
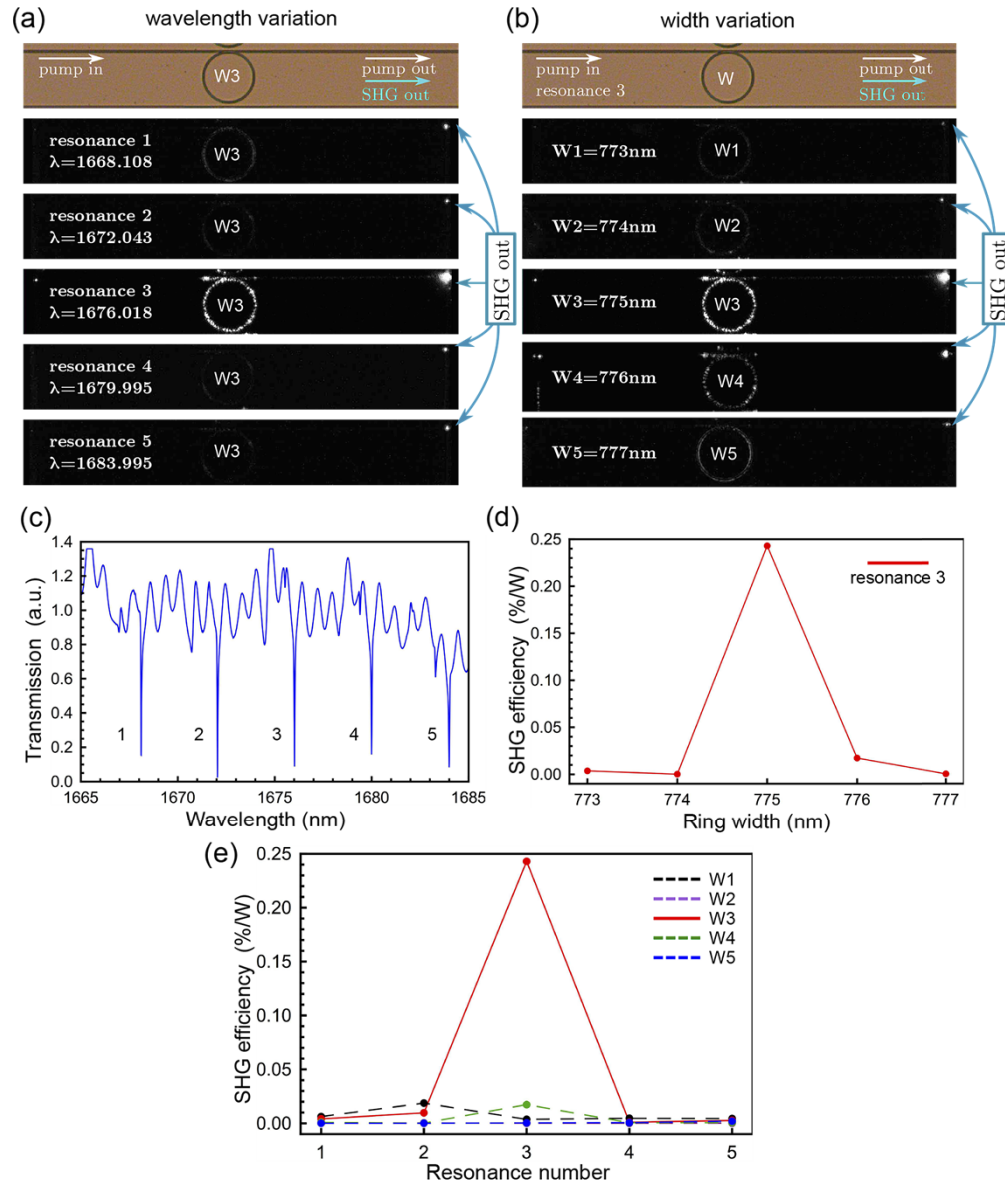
Fig. 5. (a) Spectrally-filtered optical image to highlight the second harmonic signal. The pump wavelength is tuned to the successive microring resonances corresponding to the transmission spectrum shown in (c). The waveguide width (W3) corresponds to a ring width of 775 nm. The second harmonic signal is maximum for resonance 3, as observed by scattered light at the waveguide output and on the microring. (b) Same type of measurement but with the pump wavelength tuned on resonance 3. The waveguide width varies by steps of 1 nm, as defined on the e-beam mask. The image taken for the waveguide width of 775 nm corresponds to the middle image in (a). (c) Transmission spectrum of the microring indicating the labeling of different resonances. (d) Second harmonic conversion efficiency as a function of waveguide width for a pump tuned to resonance 3. (e) Second harmonic conversion efficiency for different waveguide widths and different resonances. Only the combination of W3 and resonance 3 shows a marked enhancement of conversion efficiency.

pump and harmonic can only be reached for a narrow window of parameters because of the high-quality factors.

The conversion efficiency of 0.24%/W is significantly higher than the one reported previously in Ref. 11 for a similar platform ($\sim 1.5 \times 10^{-2}$%/W). It remains nonetheless significantly below the record values reported for AlN microring waveguides (17000%/W) [14]. Many factors contribute to the difference. We collect the harmonic signal through the same waveguide used to inject the pump. The ideal configuration would be to use a different waveguide engineered to be more efficient at shorter wavelength (waveguide width, coupling distance with the microring). The experiments reported above were performed with a TE-polarized pump (see modeling below), thus preventing to use the highest nonlinear susceptibility (d_{33}) for the III-nitrides, i.e. conversion between a TM-pump and a TM-polarized harmonic. The quality factors for the pump are lower in this work as compared to the quality factors in the Million range reported in Ref. [27]. A finer tuning of the resonant enhancement that allows the phase matching conditions to strictly coincide spectrally for pump and harmonic resonances should as well boost the conversion efficiency.

We emphasize that we could only get close to phase matching in these experiments for a pump in TE polarization. Phase matching should as well be observed for TM-polarized pump but at longer wavelengths as indicated by modeling. This is illustrated in Fig. 6 that shows the phase matching prediction for TE and TM-polarized pump modes in the case of a linear waveguide. The pump mode is TE00 or TM00 while the only available harmonic mode for phase matching is TM02 (see modal profile in Fig. 6(a)). The labeling refers to the number of nodes in the profile along the vertical and horizontal directions. The TM11 and TM10 modes do not allow for phase matching with the TE00 or TM00 pump modes. Figure 6(b) shows that the effective index for the modes can be identical around 1610 nm for the TE00 mode and the TM02 mode at half of the wavelength. This crossing of effective index lines explains that an enhanced conversion efficiency corresponding to phase matching can indeed be expected, as reported in Fig. 5. There is a shift between the modeling and the experimental observation of phase matching by about 60 nm that we attribute to a deviation of the refractive index and structural parameters accounted in the modeling as compared to their real values. Phase matching for TM00 pump mode is predicted to occur at longer wavelength (~ 40 nm) as compared to TE polarization. It is beyond the spectral range of the laser that we use in the experiments and it could not be observed. As mentioned when discussing the conversion efficiency, the harmonic conversion from TE polarizations to TM polarizations does not benefit from the highest second-order coefficient of nonlinear susceptibility.
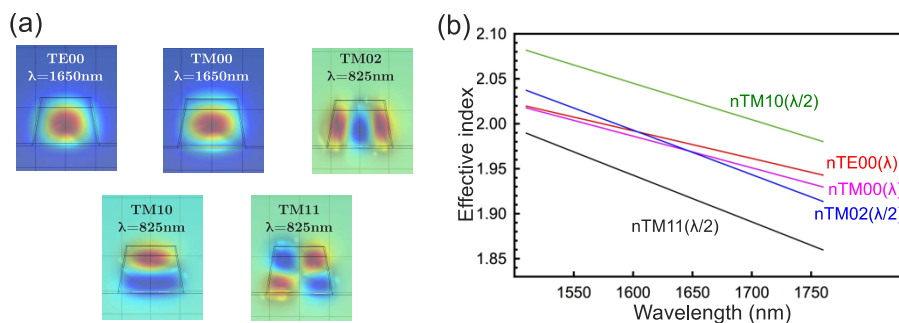
Fig. 6. (a) Mode profiles for the pump mode (TE and TM polarizations) and harmonic (TM polarization). (b) Dependence of the effective index as a function of the wavelength for the different pump and harmonic modes. The intersection of the lines between TE00 (TM00) and TM02 indicates that phase matching can be obtained.

5.   Conclusion

In this work, we have demonstrated a low-loss GaN-on-insulator platform with waveguides coupled to ring resonators exhibiting a record intrinsic quality factor of 230 000 at telecommunication wavelengths. The III-nitrides which form the core and active layers are transferred to a standard Si(100) substrate through an intermediate oxide layer that provides the optical confinement. We have demonstrated a second-harmonic conversion efficiency of 0.24%/W for continuous wave excitation. This platform opens thus new exciting possibilities for integrated nonlinear optics. It offers several advantages over similar alternative solutions: high nonlinear $\chi^{(2)}$ coefficient, wide direct band gap and possible integration with silicon photonics. Being a non-centrosymmetric material, GaN offers a $\chi^{(2)}$ nonlinearity which is the highest in the group of III-Nitride semiconductors, significantly larger than for AlN. Wide band gap materials could solve the TPA bottleneck for nonlinear photonics in the telecom range. It should be underlined that we demonstrated reliable transfer of the epitaxially-grown layers on oxide/silicon substrate. Epitaxially-grown layers have much better crystalline properties in comparison to the layers obtained by sputtering deposition. Consequently, it can both improve the nonlinear conversion and opens future opportunities for using the material active properties such as light emission. In addition, this transfer gives much better mechanical stability in comparison to suspended GaN structures and opens a possibility of future co-integration of GaN with Si photonics.

Disclosures. The authors declare no conflicts of interest.

Data availability. Data underlying the results presented in this paper are not publicly available at this time but may be obtained from the authors upon reasonable request.

References

1. S. T. Lin, Y. Y. Lin, T. D. Wang, and Y. C. Huang, "Thermal waveguide OPO," Opt. Express **18**(2), 1323–1329 (2010).
2. H. Jung, C. Xiong, K. Y. Fong, X. F. Zhang, and H. X. Tang, "Optical frequency comb generation from aluminum nitride microring resonator," Opt. Lett. **38**(15), 2810–2813 (2013).
3. S. Tanzilli, W. Tittel, H. De Riedmatten, H. Zbinden, P. Baldi, M. De Micheli, D. B. Ostrowsky, and N. Gisin, "PPLN waveguide for quantum communication," The European Physical Journal D-Atomic, Molecular Optical and Plasma Physics **18**(2), 155–160 (2002).
4. J. Lu, J. B. Surya, X. Liu, A. W. Bruch, Z. Gong, Y. Xu, and H. X. Tang, "Periodically poled thin-film lithium niobate microring resonators with a second-harmonic generation efficiency of 250,000%/W," Optica **6**(12), 1455–1460 (2019).
5. P. S. Kuo, J. Bravo-Abad, and G. S. Solomon, "Second-harmonic generation using-quasi-phasematching in a GaAs whispering-gallery-mode microcavity," Nat. Commun. **5**(1), 3109 (2014).
6. D. P. Lake, M. Mitchell, H. Jayakumar, L. F. dos Santos, D. Curic, and P. E. Barclay, "Efficient telecom to visible wavelength conversion in doubly resonant gallium phosphide microdisks," Appl. Phys. Lett. **108**(3), 031109 (2016).
7. C. Xiong, W. Pernice, K. Ryu, C. Schuck, K. Y. Fong, T. Palacios, and H. X. Tang, "Integrated GaN photonic circuits on silicon (100) for second harmonic generation," Opt. Express **19**(11), 10462–10470 (2011).
8. X. Guo, C.-L. Zou, C. Schuck, H. Jung, R. Cheng, and H. X. Tang, "Parametric down-conversion photon-pair source on a nanophotonic chip," Light: Sci. Appl. **6**(5), e16249 (2017).
9. X. Liu, C. Sun, B. Xiong, L. Wang, J. Wang, Y. Han, Z. Hao, H. Li, Y. Luo, J. Yan, T. Wei, Y. Zhang, and J. Wang, "Aluminum nitride-on-sapphire platform for integrated high-Q microresonators," Opt. Express **25**(2), 587–594 (2017).

10. J. Liu, H. Weng, A. A. Afridi, J. Li, J. Dai, X. Ma, H. Long, Y. Zhang, Q. Lu, J. F. Donegan, and W. Guo, "Photolithography allows high-Q AlN microresonators for near octave-spanning frequency comb and harmonic generation," Opt. Express **28**(13), 19270 (2020).

11. G. T. Reed and A. P. Knights, "*Silicon photonics: An introduction*," Wiley, ISBN: 978-0-470-87034-1 (2004).

12. X. Guo, C.-L. Zou, and H. X. Tang, "Second-harmonic generation in aluminum nitride microrings with 2500%/W conversion efficiency," Optica **3**(10), 1126–1131 (2016).

13. A. W. Bruch, X. Liu, J. B. Surya, C.-L. Zou, and H. X. Tang, "On-chip χ(2) microring optical parametric oscillator," Optica **6**(10), 1361–1366 (2019).

14. A. W. Bruch, X. Liu, X. Guo, J. B. Surya, Z. Gong, L. Zhang, J. Wang, J. Yan, and H. X. Tang, "17 000%/W second-harmonic conversion efficiency in single-crystalline aluminum nitride microresonators," Appl. Phys. Lett. **113**(13), 131102 (2018).

15. I. Roland, Y. Zeng, Z. Han, X. Checoury, C. Blin, M. El Kurdi, A. Ghrib, S. Sauvage, B. Gayral, C. Brimont, T. Guillet, F. Semond, and P. Boucaud, "Near-infrared gallium nitride two-dimensional photonic crystal platform on silicon," Appl. Phys. Lett. **105**(1), 011104 (2014).

16. I. Roland, M. Gromovyi, Y. Zeng, M. El Kurdi, S. Sauvage, C. Brimont, T. Guillet, B. Gayral, F. Semond, J. Y. Duboz, M. de Micheli, X. Checoury, and P. Boucaud, "Phase-matched second harmonic generation with on-chip GaN-on-Si microdisks," Sci. Rep. **6**(1), 34191 (2016).

17. F. Tabataba-Vakili, L. Doyennette, C. Brimont, T. Guillet, S. Rennesson, E. Frayssinet, B. Damilano, J.-Y. Duboz, F. Semond, I. Roland, M. El Kurdi, X. Checoury, S. Sauvage, B. Gayral, and P. Boucaud, "Blue microlasers integrated on a photonic platform on silicon," ACS Photonics **5**(9), 3643–3648 (2018).

18. N. Vico Triviño, R. Butté, J.-F. Carlin, and N. Grandjean, "Continuous Wave Blue Lasing in III-Nitride Nanobeam Cavity on Silicon," Nano Lett. **15**(2), 1259–1263 (2015).

19. F. P. Payne and J. P. R. Lacey, "A theoretical analysis of scattering loss from planar optical waveguides," Opt. Quantum Electron. **26**(10), 977–986 (1994).

20. M. Gromovyi, J. Brault, A. Courville, S. Rennesson, F. Semond, G. Feuillet, P. Baldi, P. Boucaud, J.-Y. Duboz, and M. P. de Micheli, "Efficient second harmonic generation in planar GaN waveguides," Opt. Express **25**(19), 23035 (2017).

21. M. Borselli, T. J. Johnson, and O. Painter, "Beyond the Rayleigh scattering limit in high-Q silicon microdisks: theory and experiment," Opt. Express **13**(5), 1515 (2005).

22. Y. Zheng, C. Sun, B. Xiong, L. Wang, Z. Hao, J. Wang, Y. Han, H. Li, Y. Jiadong, and Y. Luo, "Integrated Gallium Nitride Nonlinear Photonics," Laser & Photonics Review **16**(1), 2100071 (2022).

23. Y. Zheng, C. Sun, B. Xiong, L. Wang, Z. Hao, J. Wang, Y. Han, H. Li, Y. Jiadong, and Y. Luo, "High Q Microresonators Based on Epitaxial GaN Film," *Conference on Lasers and Electro-Optics OSA Technical Digest* (Optical Society of America, 2020), paper SM4R.2, https://www.osapublishing.org/abstract.cfm?uri=CLEO_SI-2020-SM4R.2.

24. E. Stassen, M. Pu, E. V. Semenova, E. Zavarin, W. Lundin, and K. Yvind, "High-confinement gallium nitride-on-sapphire waveguides for integrated nonlinear photonics," Opt. Lett. **44**(5), 1064 (2019).

25. H. Zi, Y.-F. Cheung, B. Damilano, E. Frayssinet, B. Alloing, J.-Y. Duboz, P. Boucaud, F. Semond, and H. W. Choi, "Influence of surface roughness on the lasing characteristics of optically pumped thin-film GaN microdisks," Opt. Lett. **47**(6), 1521 (2022).

26. B. Wang, E. Sakat, E. Herth, M. Gromovyi, A. Bjelajac, J. Chaste, G. Patriarche, P. Boucaud, F. Boeuf, N. Pauc, V. Calvo, J. Chrétien, M. Frauenrath, A. Chelnokov, V. Reboud, J.-M. Hartmann, and M. El Kurdi, "GeSnOI mid-infrared laser technology," Light Sci Appl **10**(1), 232 (2021).